Table S1: Perturbed parameters in the GC3.05-PPE. Descriptions are from, and more detail of parameters can be found in Murphy et al. 2018.

Perturbed parameter	Name	Description
Convection		
ent_fac_dp	Deep entrainment amplitude	Controls the shape of the mass flux and sensitivity of deep convection to relative humidity to deep entrainment.
ent_fac_md	Mid entrainment amplitude	Controls the shape of the mass flux and the sensitivity of mid-level convection to relative humidity to mid-level entrainment.
amdet_fac	Mixing detrainment	Controls the rate of humidification of the atmosphere and the shape of the convective heating profile.
r_det	Coefficient for adaptive detrainment	Decrease of mass flux with height under decreasing parcel buoyancy.
cca_md_knob, cca_dp_knob	Convective core radiative effects	Controls how much deep and mid-level convective core gets seen by radiation.
cca_sh_knob	Shallow convection core radiative effects	Controls how much shallow convection gets seen by radiation.
mparwtr	Maximum condensate	The maximum condensate a convective parcel can hold before it is converted to precipitation.
qlmin	Minimum critical cloud condensate	The minimum value of the function that defines the maximum amount of condensate a convective parcel can hold before it is converted to precipitation.
Gravity wave drag		
gwd_frc	Critical Froude number	Determines the cut-off mountain height and the depth of the blocked flow layer around sub-grid mountains.
fbcd	Flow blocking drag coefficient	Determines the size of the low-level drag associated with flow blocking effects by sub-grid mountains.
gwd_fsat	Inverse critical Froude number for wave saturation	Determines the amplitude at which mountain waves generated by sub-grid orography will break, and exert a drag on the flow.
gsharp	Mountain wave amplitude	Determines the amplitude of the mountain waves generated by sub-grid orography.
orog_drag_param	Drag coefficient for turbulent form drag	Determines the size of the form drag exerted on flow by small-scale sub-grid hills.
nsigma	Scaling factor applied to the standard deviation of sub-grid mountain heights.	Determines the local assumed sub-grid orography height which is used in the gravity wave drag scheme.
Boundary layer		
g0	Flux profile parameter	Used in the definition of stability functions.
ricrit = 10.0 / g0	Critical Richardson number	Value of Richardson number below which air becomes dynamically unstable and turbulent.
a_ent_1	Cloud-top entrainment rate.	Used in entrainment rate calculation.
g1	Cloud-top diffusion	Used in cloud-top diffusion calculation.
zhloc_depth_fac	Threshold fraction of the cloud layer depth	Fractional height into cloud layer for which Ri-based boundary layer depth can diagnose shear dominated layer.
par_mexcla	Neutral mixing length	Mixing length for fluid parcels under neutral stability conditions.
lambda_min	Minimum value of mixing length.	

dec_thresh_cld, dec_thresh_cloud2cu	Decoupling threshold for cloud boundary layers.	
forced_cub_fac	Mixing factor applied to the in-cloud water content of forced cumulus clouds.	Determines the fraction of diagnosed adiabatic water content of forced cumulus clouds which is allowed to remain.
Clouds and cloud radiation		
dbsdtbs_turb_0	Cloud erosion rate	Determines the rate which un-resolved sub-grid motions mix clear and cloudy air.
two_d_fsd_factor	Scaling to make sub-grid cloud condensate variance to cloud cover and convective activity to dimensional.	Makes the cloud water variability around the grid box average a two dimensional relationship, based on 1-d empirical relationship.
dp_corr_strat	Decorrelation scale pressure	Determines the vertical overlap between clouds in the sub-column in the cloud generator used to calculate the radiative impact of clouds.
ice_width	Ice width	Determines the amount of ice water content that corresponds to a factor of two reduction in the width of the vapour distribution in the liquid-free part of the grid box.
Cloud microphysics		
c_r_correl	Cloud-rain correlation coefficient	Determines the sub-grid correlation between cloud and precipitation.
m_ci	Ice fall speed	Scaling factor for the ice fall speed.
ai	Precursor coefficient in the mass-diameter relationship for ice.	Changing ai has the effect of changing the density of ice.
x1r		Controls the shape of the PSD for raindrops.
ar	Aspect ratio of ice particles.	Used to calculate the depositional capacitance of ice crystals which affects how efficiently they grow by depleting water vapour.
mp_dz_scal	Vertical scale in mixed-phase turbulent production of supercooled liquid water.	Vertical length scale over which the turbulence acts to produce supercooled water.
Aerosols		
ps_anth_so2_emiss	Anthropogenic SO_2 emission flux	Direct scaling of anthropogenic SO_2 emission flux.
ps_dry_so2_veloc	Dry deposition rate of SO_2	Scaling factor for the dry deposition rate which removes SO_2 from lowest levels through deposition according to land surface type and prevailing wind speed.
ps_sigma_updraught	Scaling of the standard deviation use to define the pdf of updraught velocity	Relates the activation of aerosols to cloud droplets to the standard deviation used to define the pdf of updraught velocity.
biom_aer_ems_scaling	Scaling of emission flux from biomass burning	Direct scaling of emission flux.
ps_natl_ss_emiss	Scaling of emission flux from sea spray	Direct scaling of emissions flux.
pd_natl_dms_emiss	Dimethyl-sulphide emission flux	Direct scaling of emissions flux.
ps_acc_cor_scav	Scavenging rate in the coarse and accumulation modes.	Scaling of the scavenging rate calculated in the model.

ps_cloud-pH	pH of cloud drops	Controls the in-cloud SO_4 production dependent on SO_2 availability.
Land surface and snow		
u10_max_coare	Maximum wind speed used in the Coupled Ocean-Atmosphere Response Experiment (COARE) algorithm	This is the highest wind speed used in calculating the Charnock coefficient in the COARE algorithm.
r0	Grain size of fresh snow	The grain size of fresh snow is set to this value.
rho_snow_fresh	Fresh snow density	The density of fresh snow.
tupp_io	Upper value about 4K above the optimal value for photosynthesis	Temperatures above the optimal value for photosynthesis will drive a decline in photosynthesis.
f0_io	Maximum ratio of internal to external CO_2	Controls the gradient of CO_2 between plant stomata and the ambient air.
nl0-io	Top leaf nitrogen concentration	Defines the top leaf ration of nitrogen to carbon. Plant photosynthesis is defined in the model to be proportional to the leaf nitrogen concentration.
rootd_ft_io	Root depth	Controls the depth to which soil moisture is available.
psm	Scaling factor for critical and saturation levels for soil moisture towards wilt level	This pair of parameters control the critical and saturated volumetric soil moisture thresholds. The critical threshold controls the level above which evapotranspiration is no longer soil moisture dependent.

Figure S1: 1860 to 1975 aerosol ERF for individual ensemble members. Global mean aerosol ERF, and northern hemisphere (0 to 60 °N) – southern hemisphere (0 to 60 °S) are shown above each ensemble member. The ensemble mean and standard deviation are shown in the first two plots.

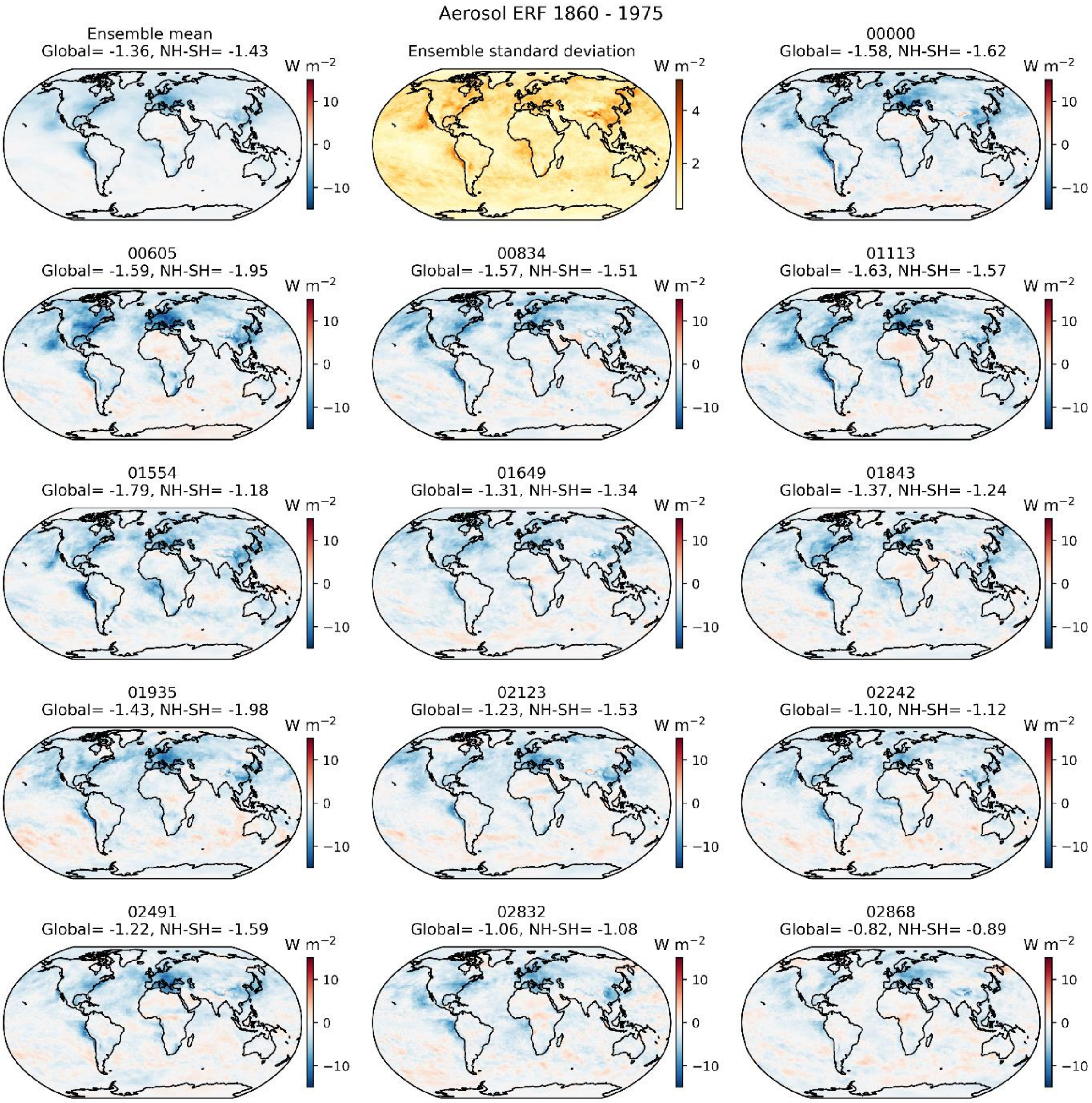

Figure S2: 1860 to 2005 aerosol ERF for individual ensemble members. Global mean aerosol ERF, and northern hemisphere (0 to 60 °N) – southern hemisphere (0 to 60 °S) are shown above each ensemble member. The ensemble mean and standard deviation are shown in the first two plots.

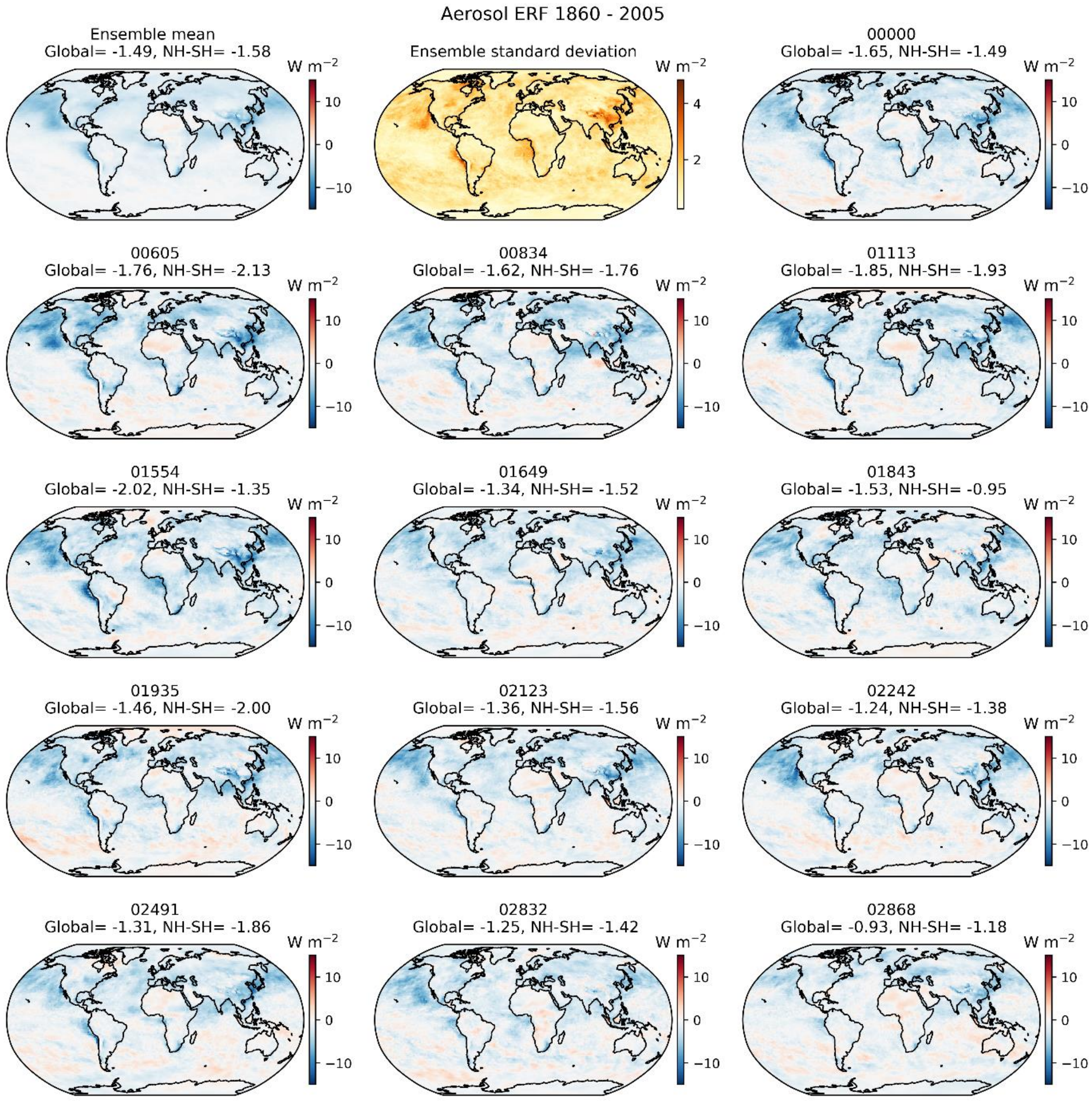

Figure S3: Time series of Φ_{ITCZ} anomaly against a 1950 to 2000 reference period with no rolling mean for global (top, 0 - 360 ° longitude), Atlantic (middle, -70 - 10 ° longitude) and Pacific regional means (150 - 285 ° longitude). Historical emissions are shown in black, RCP8.5 in red and RCP2.6 in blue. Major volcanic eruptions are marked with grey vertical lines. The ensemble mean is shown by the darker line, and the individual ensemble members in the lighter lines.

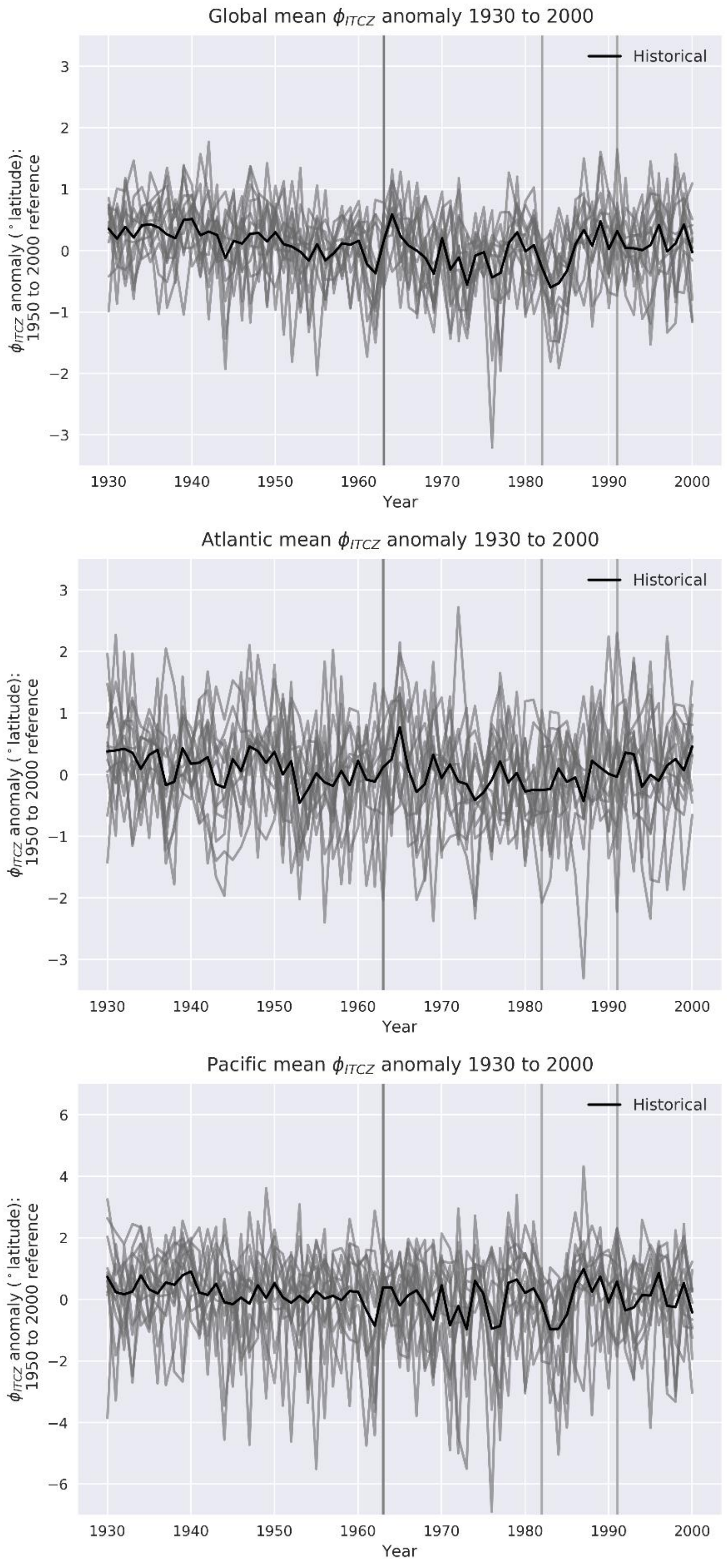

Figure S4: Time series of the inter-hemispheric (60 °S to 60 °N, NH-SH) surface temperature anomaly against a 1950 to 2000 reference period with a 5-year rolling mean for global (top, 0 - 360 ° longitude), Atlantic (middle, -70 - 10 ° longitude) and Pacific regional means (150 - 285 ° longitude). Historical emissions are shown in black, RCP8.5 in red and RCP2.6 in blue. Major volcanic eruptions are marked with grey vertical lines. The ensemble mean is shown by the darker line, and the individual ensemble members in the lighter lines.

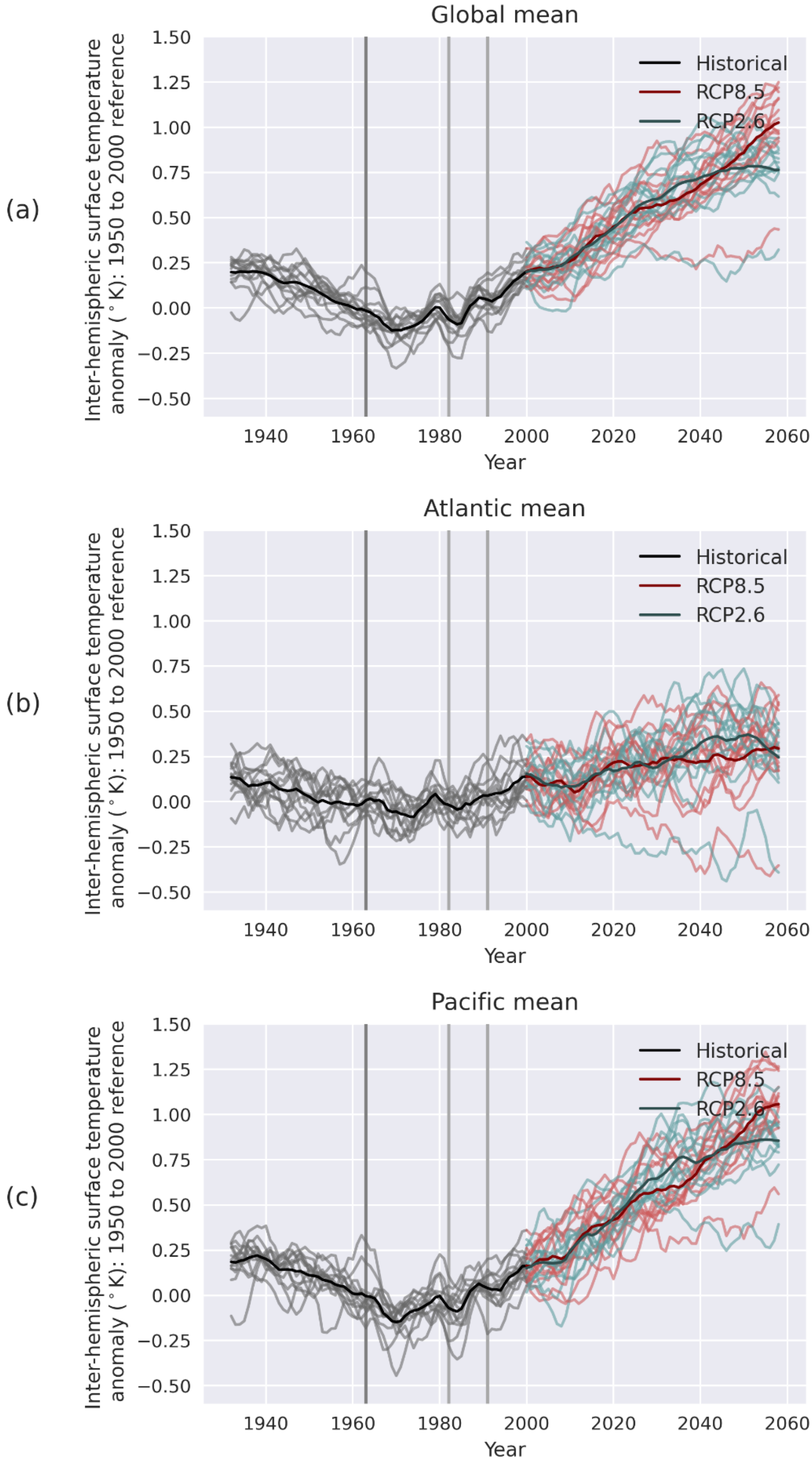

Figure S5: Time series of the inter-hemispheric (60 °S to 60 °N, NH-SH) total AOD anomaly against a 1950 to 2000 reference period with a 5-year rolling mean for global (top, 0 - 360 ° longitude), Atlantic (middle, -70 - 10 ° longitude) and Pacific regional means (150 - 285 ° longitude). Historical emissions are shown in black and RCP8.5 in red. Major volcanic eruptions are marked with grey vertical lines. The ensemble mean is shown by the darker line, and the individual ensemble members in the lighter lines.

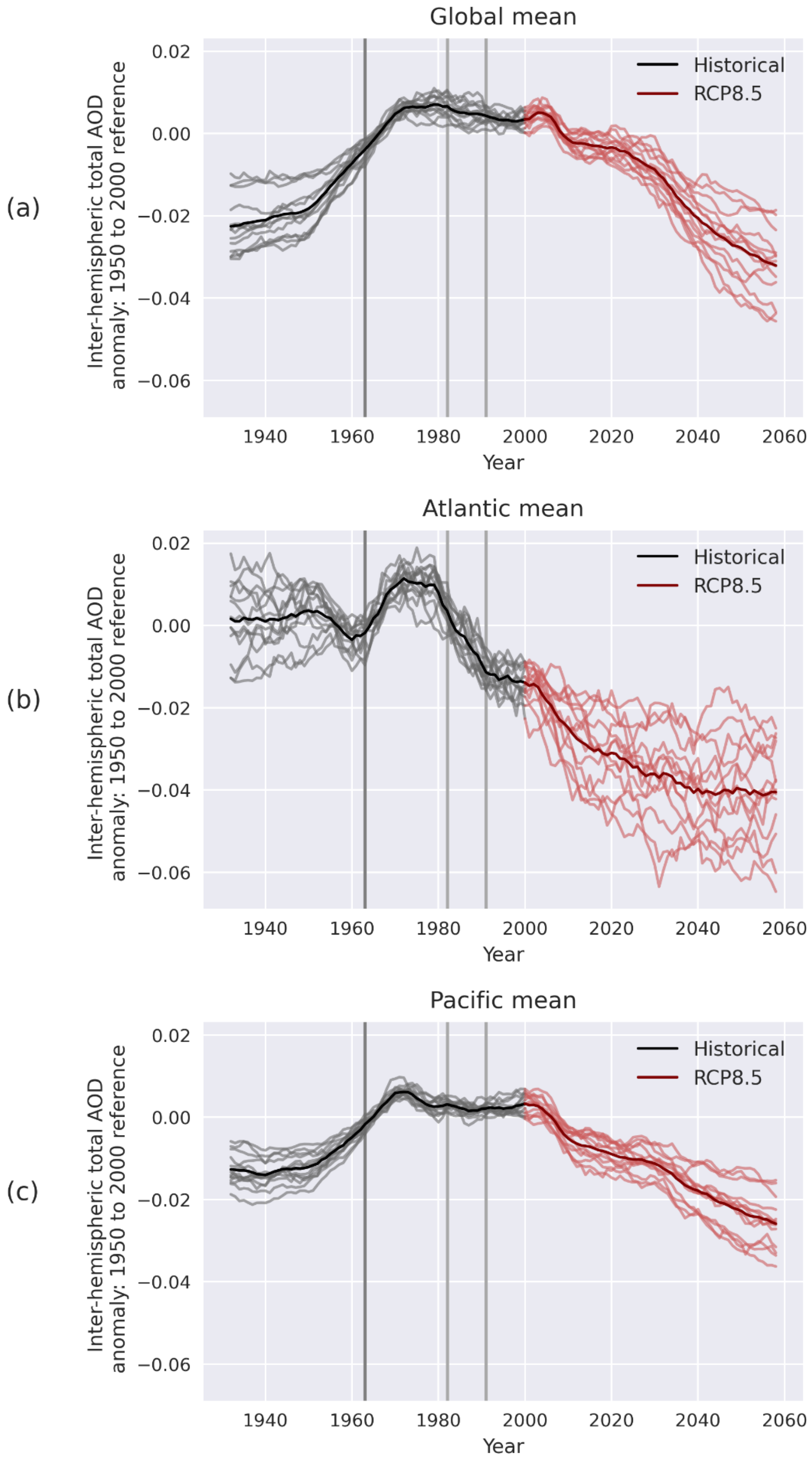

Figure S6: Scatter plot of trend in 5-year rolling mean Φ_{ITCZ} in 1950 to 1985 (top) against ocean-only inter-hemispheric (60 °S to 60 °N) trend in surface air temperature (top), total implied radiative forcing (middle) and 1860 to 1975 aerosol ERF (bottom) for global (left), Atlantic (middle) and Pacific (right) regional means. Individual ensemble members are coloured according to legend. Spearman's rank correlation coefficient is shown at top left of each plot.

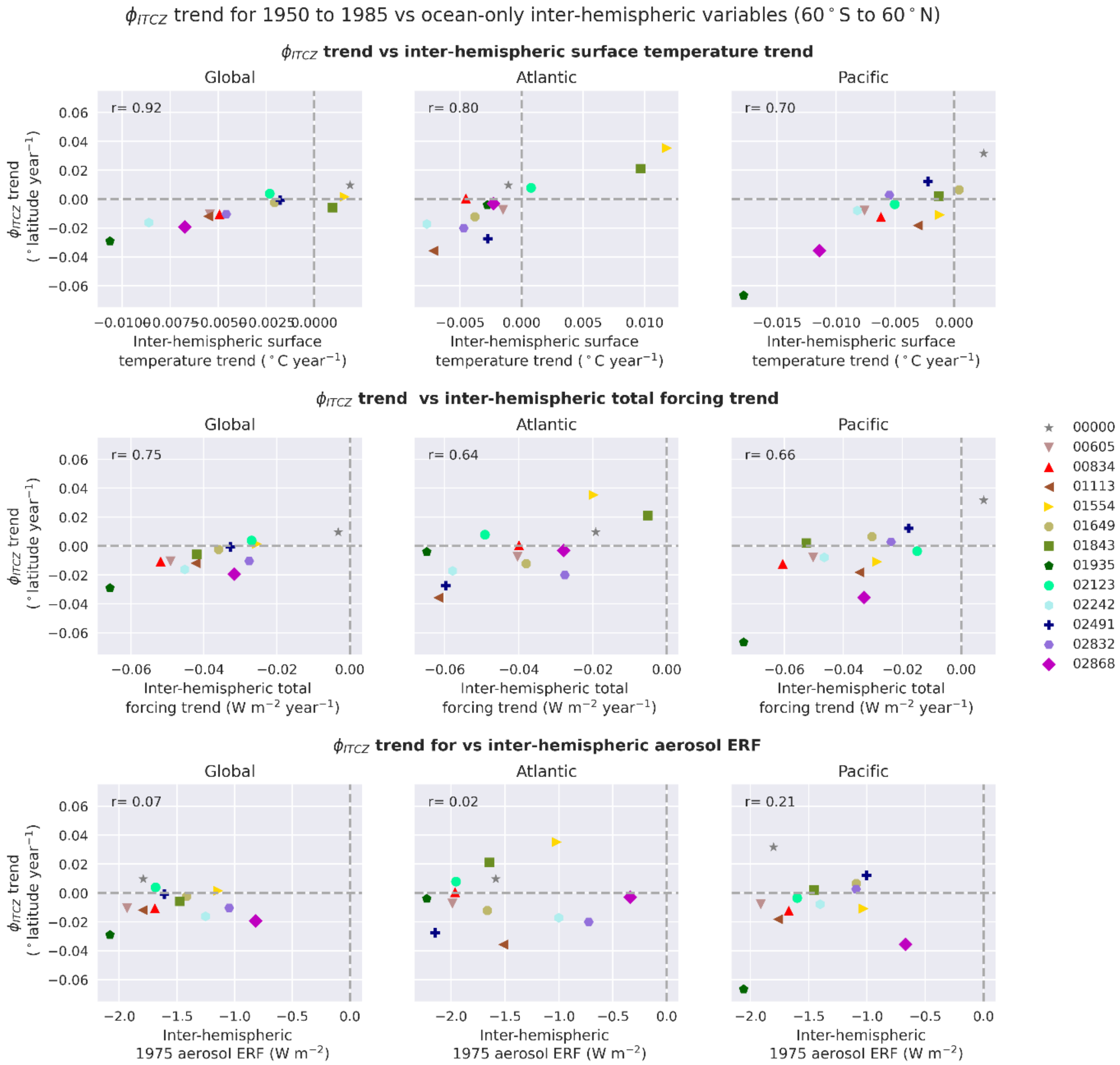

Table S2. Table of Spearman's rank correlation coefficients for the trend in global mean 5-year rolling mean Φ_{ITCZ} and ocean-only inter-hemispheric variables shown in Figure 3 for the time periods: 1950 to 1985, 1950 to 1980, 1940 to 1985, 1940 to 1980 and 1940 to 1975.

Time period	Correlation with the trend in inter-hemispheric surface air temperature (°C $year^{-1}$)	Correlation with the trend in inter-hemispheric implied total forcing (W m^{-2} $year^{-1}$)	Inter-hemispheric 1860 to 1975 aerosol ERF (W m^{-2})
1950 to 1985 (shown)	r= 0.92	r= 0.75	r= 0.07
1950 to 1980	r= 0.69	r= 0.66	r= 0.14
1940 to 1985	r= 0.19	r= 0.55	r= -0.08
1940 to 1980	r= -0.03	r= 0.49	r= -0.10
1940 to 1975	r= 0.26	r= 0.63	r= -0.35

Figure S7: Scatter plot of (top) 1950 to 1985 inter-hemispheric surface temperature trend against 1860 to 1975 aerosol ERF and (middle, bottom) 2006 to 2060 inter-hemispheric surface temperature trend against 1860 to 2005 aerosol ERF for global (left), Atlantic (middle) and Pacific (right) regional means. Individual ensemble members are coloured according to legend. Spearman's correlation coefficient is shown at top left of each plot.

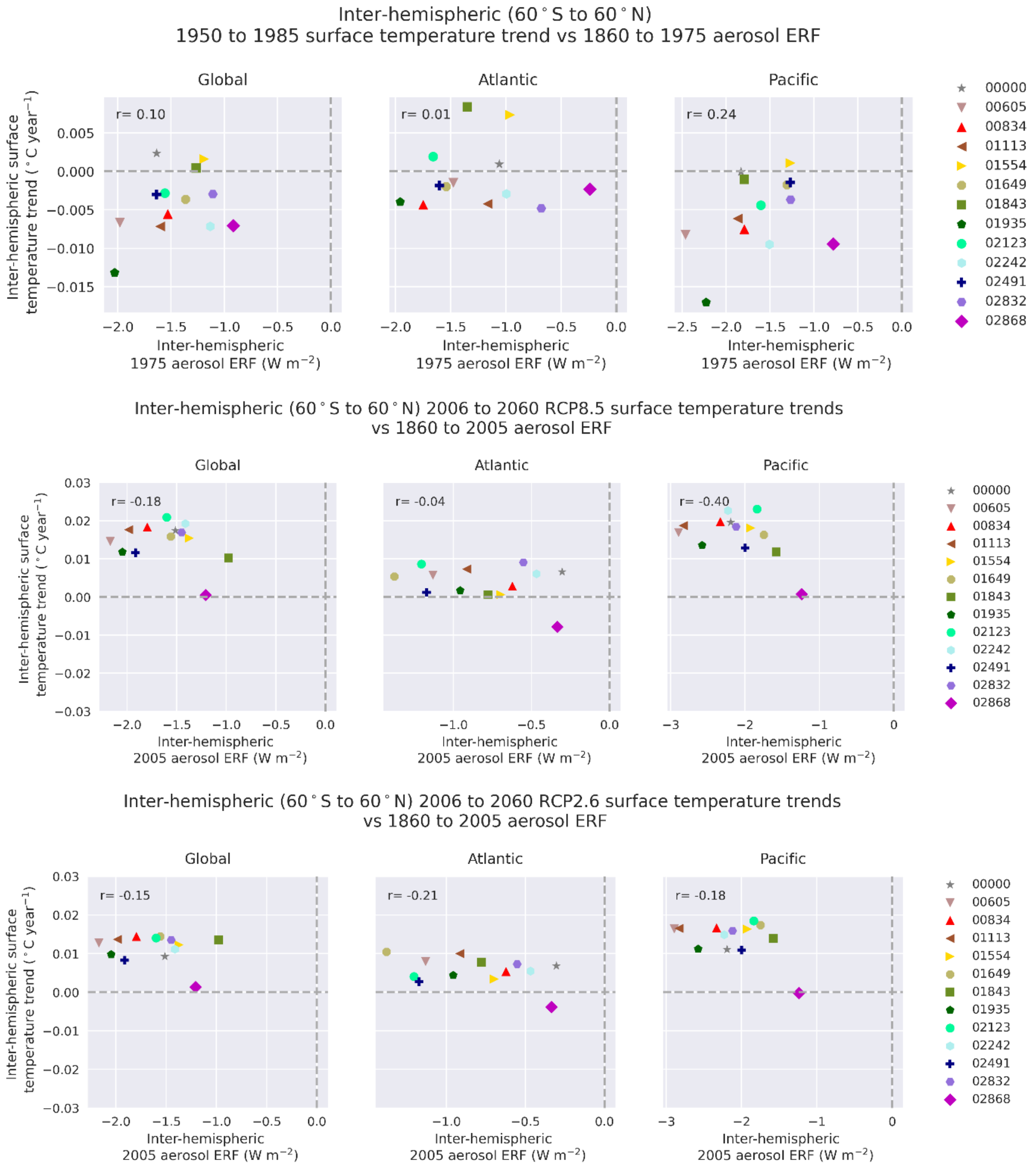

Figure S8: Scatter plot of the 1950 to 1985 trend in 5-year rolling mean Φ_{ITCZ} against inter-hemispheric top of atmosphere outgoing shortwave flux (rsut) (0 to 60 °S and ° N latitude) for global (left), Atlantic (middle) and Pacific (right) regional means. Individual ensemble members are coloured according to legend. Spearman's rank correlation coefficient is shown at top left of each plot.

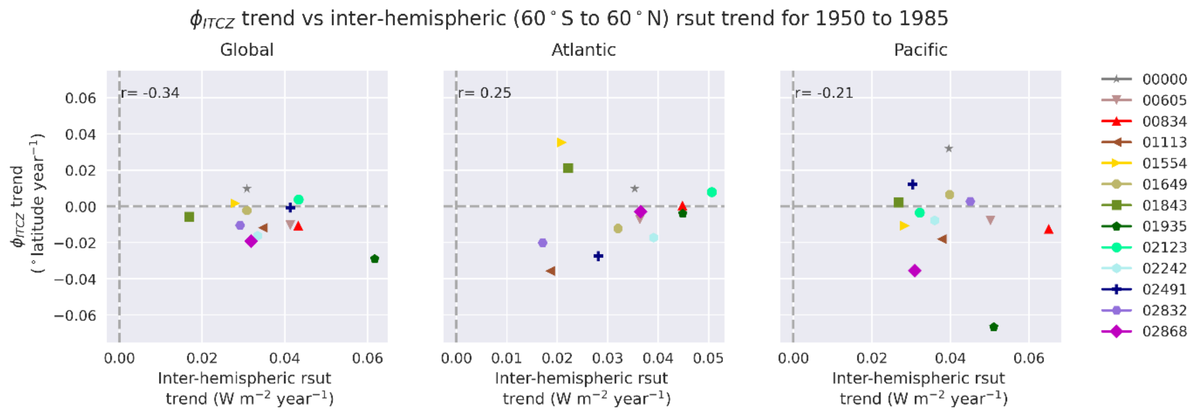

Figure S9: Scatter plot of the 1950 to 1985 trend in 5-year rolling mean Φ_{ITCZ} against inter-hemispheric (0 to 60 ° S and ° N latitude) total AOD (top) and dust AOD (bottom) for global (left), Atlantic (middle) and Pacific (right) regional means. Individual ensemble members are coloured according to legend. Spearman's rank correlation coefficient is shown at top left of each plot.

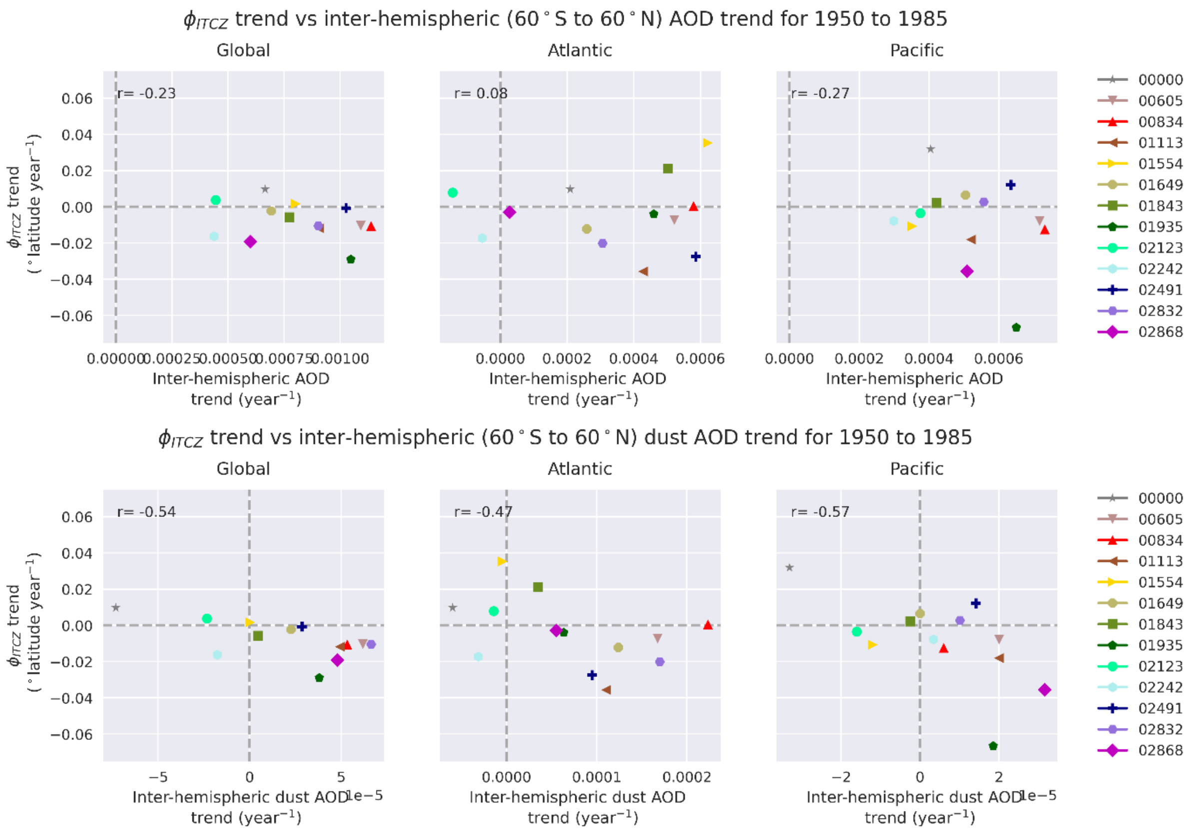

Figure S10: Scatter plot of 1950 to 1985 and 1940 to 1975 trend in 5-year rolling mean Φ_{ITCZ} against trend in global inter-hemispheric (90 °S to 90 °N) implied forcing from shortwave non-cloud interactions and cloud interactions for global (left), Atlantic (middle) and Pacific (right) regional. Spearman's rank correlation coefficient is shown at top left of each plot.

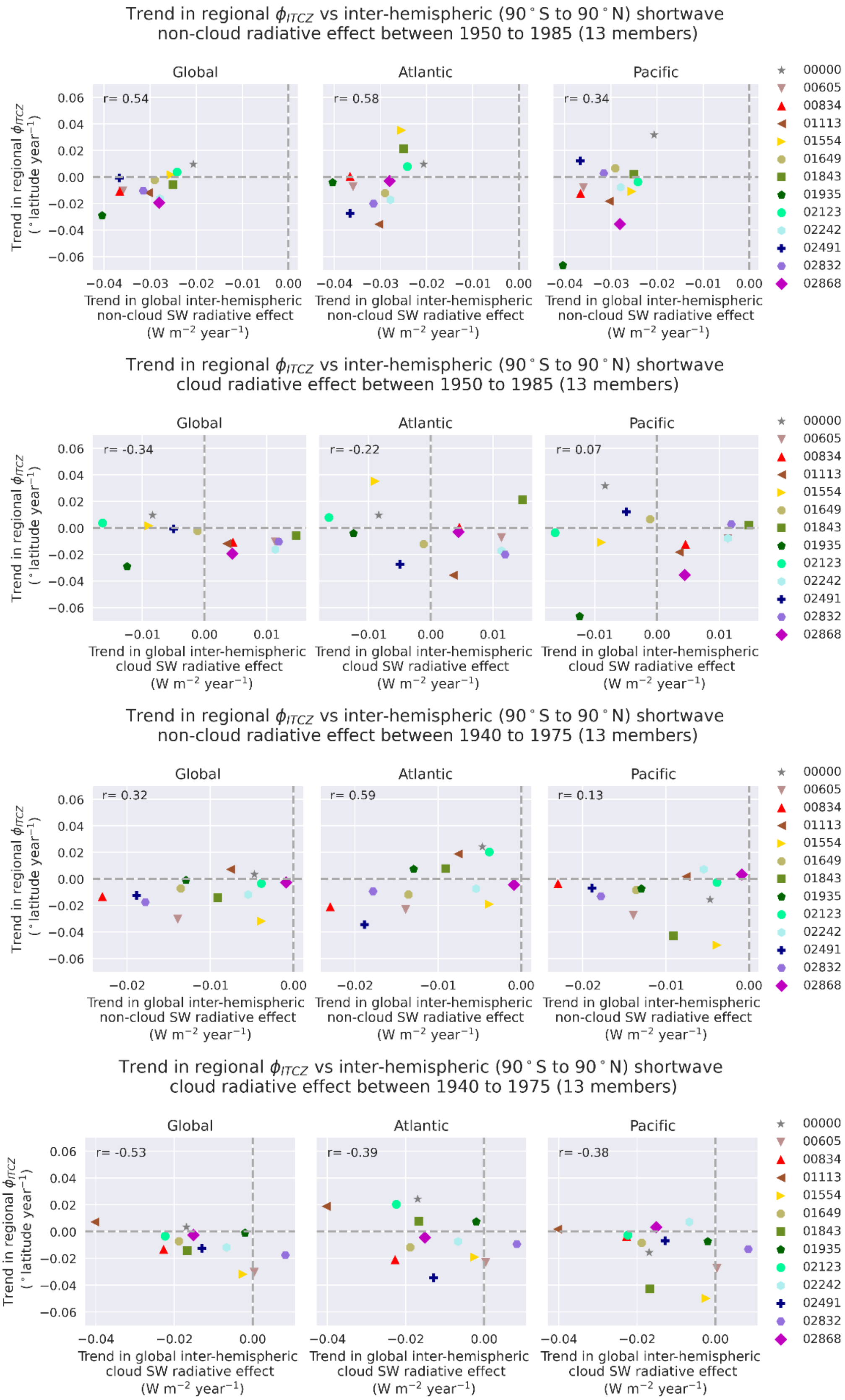

Figure S11: Plots of the parameters that have a Spearman's rank correlation coefficient or r > 0.5 with the trend in 5-year rolling mean Φ_{ITCZ} in 1950 to 1985 in global (top), Atlantic (middle) and Pacific (bottom) regional means. Individual ensemble members are coloured according to legend. Negative relationships are shown in pink and positive in green. Definitions of parameters are in Table S1.

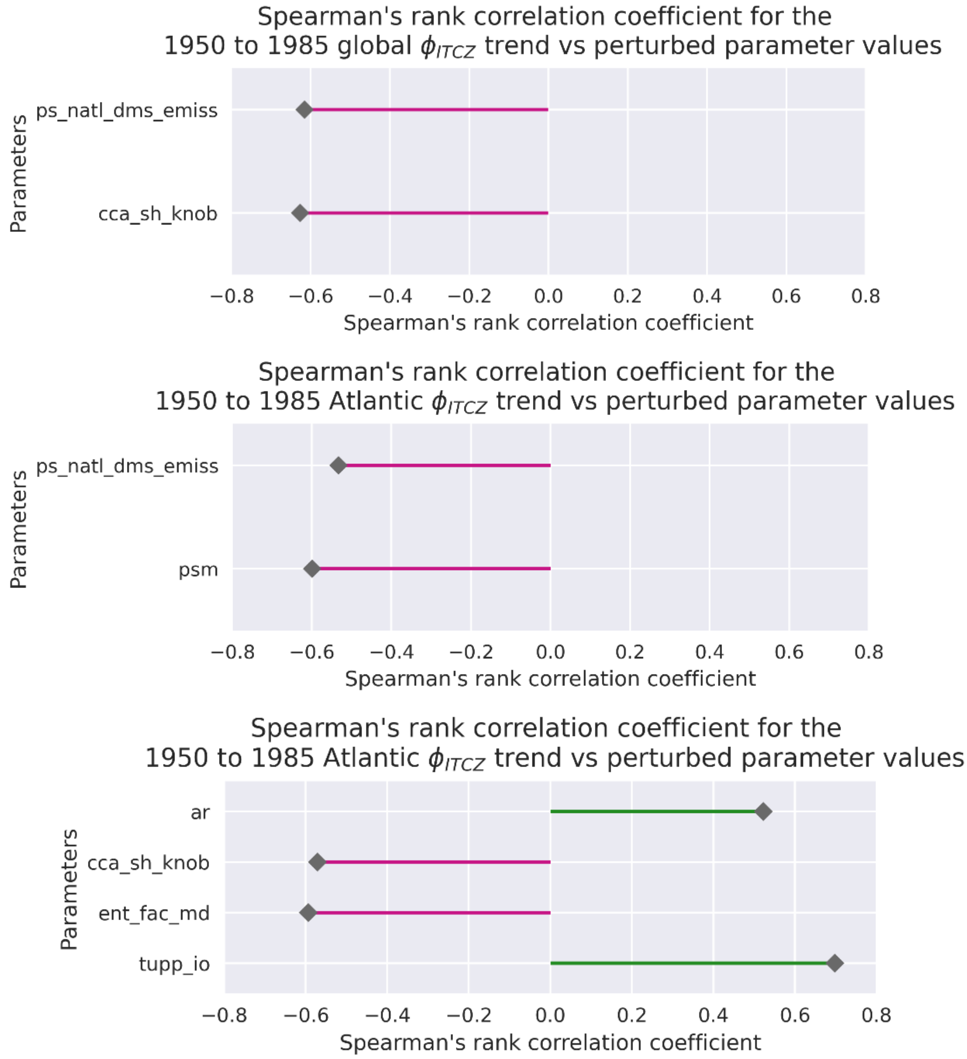

Text S1. Tropical precipitation shifts were also calculated based on the methodology in Allen et al. 2015 in order to compare the spread in our single-model PPE to a multi-model ensemble. First, the annual precipitation anomaly is calculated against a 1961 – 1990 base period. This methodology then defines tropical precipitation shifts (mm decade^{-1}) as the difference between area-weighted northern hemisphere (0 – 20 °N) and southern hemispheric (0 – 20 °S) regional means over land and ocean. The Atlantic region is defined (75 °W – 30 °E) and the Pacific region as (30 °E – 75 °W). The trend over 1950 – 1985 is calculated from the 5-year rolling mean of this metric.

Figure S12. The 1950 to 1985 trend in the tropical precipitation metric (NH-SH PRECT / mm decade^{-1}) defined in Text S1 over land and ocean for the three regional means.

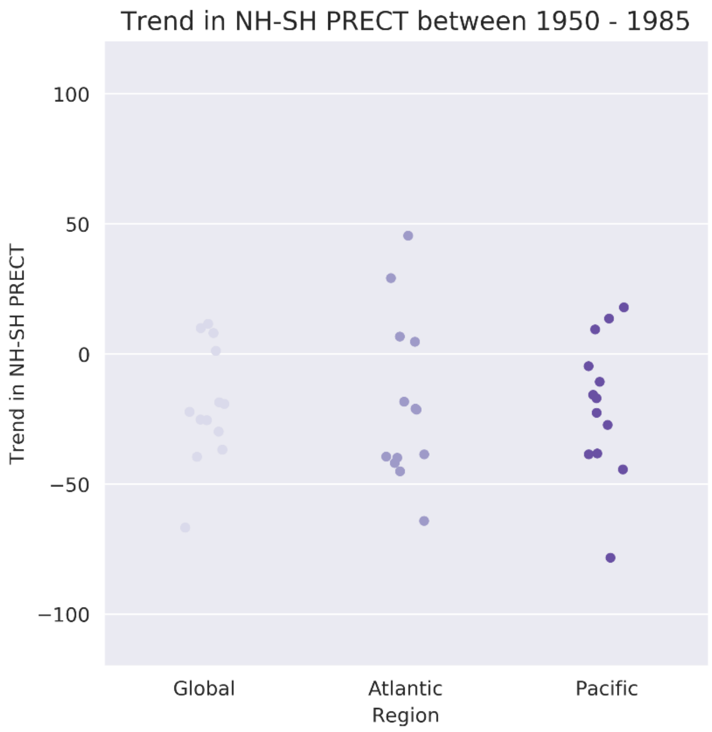

Figure S13: Scatter plot of trend in 5-year rolling mean Φ_{ITCZ} in 2006 to 2060 (top) against ocean-only inter-hemispheric (60 °S to 60 °N) trend in surface air temperature (top), implied total forcing (middle) and 1860 to 1975 aerosol ERF (bottom) for global (left), Atlantic (middle) and Pacific (right) regional means. Individual ensemble members are coloured according to legend. The Spearman's rank correlation coefficient is shown at top left of each plot. For the top row, RCP8.5 is red, RCP2.6 is teal, and the scenarios combined is black.

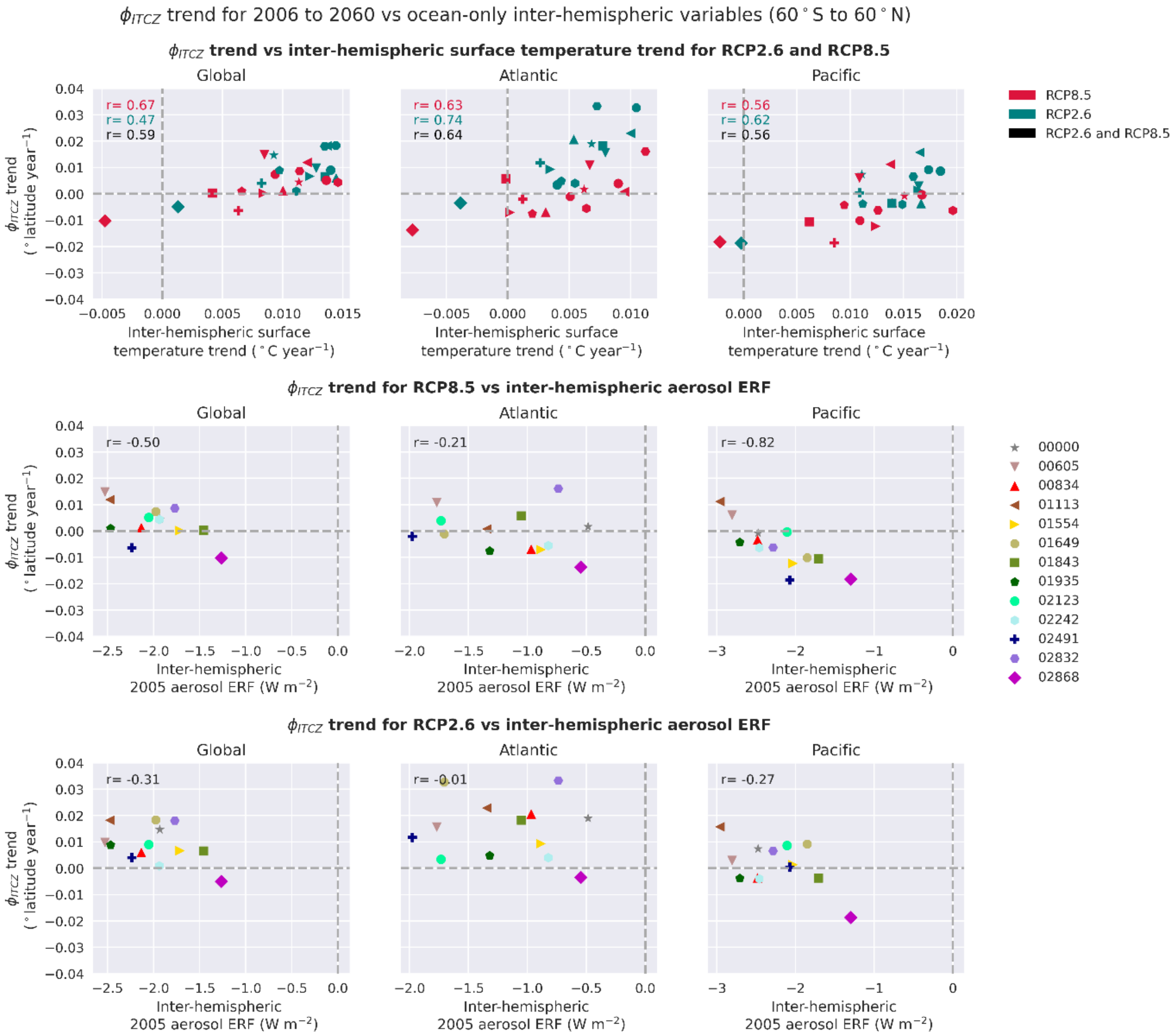

Figure S14. Time series of trend in 5-year rolling mean Φ_{ITCZ} in 2006 to 2040 for RCP8.5, the internal variability is estimated from HadGEM3-GC3.1 (historical and SSP5-8.5) ensemble. This figure tests how the trend over a future time period of comparable size to the historical time period influences the range of trends in tropical precipitation across the ensemble.

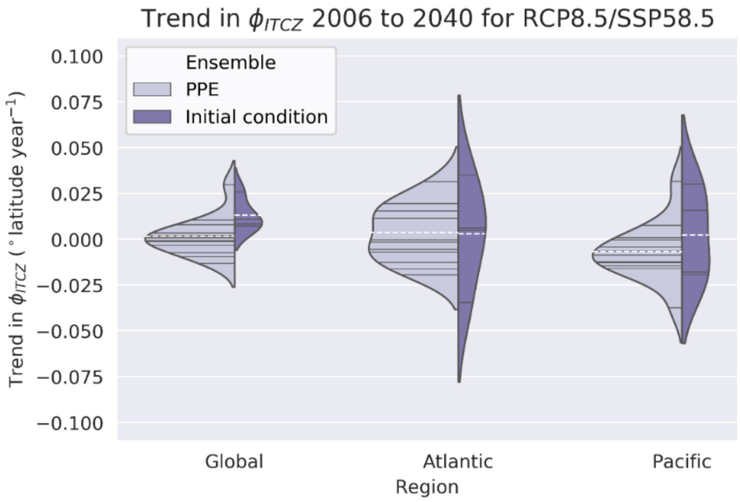

References

Allen, R. J., Evan, A. T. and Booth, B. B. B.: Interhemispheric aerosol radiative forcing and tropical precipitation shifts during the late Twentieth Century, J. Clim., 28(20), 8219–8246, doi:10.1175/JCLI-D-15-0148.1, 2015.

Murphy, J. M., Harris, G. R., Sexton, D. M. H., Kendon, E. J., Bett, P. E., Clark, R. T., Eagle, K. E., Fosser, G., Fung, F., Lowe, J. A., McDonald, R. E., McInnes, R. N., McSweeney, C. F., Mitchell, J. F. B., Rostron, J. W., Thornton, H. E., Tucker, S. and Yamazaki, K.: UKCP18: Land Projections Science Report., 2018.